Bio-Inspired Degradable Polyethylenimine/Calcium Phosphate Micro-/Nano Composites for Transient Ultrasound and Photoluminescence Imaging

Tengyu He[a], David G. Bradley[b], Ming Xu[c], Shu-Ting Ko[a], Baiyan Qi[a], Yi Li[c], Yong Cheng[c], Zhicheng Jin[c], Jiajing Zhou[c], Lekshmi Sasi[c], Lei Fu[c], Zhuohong Wu[c], Jingcheng Zhou[c], Wonjun Yim[a], Yu-Ci Chang[a], John V. Hanna[b], Jian Luo[a, c], Jesse V. Jokerst[a, c, d, *]

[a] Materials Science and Engineering Program, University of California San Diego, 9500 Gilman Drive, La Jolla, California, 92093, United States
[b] Department of Physics, University of Warwick, Coventry, CV4 7AL, UK
[c] Department of NanoEngineering, University of California San Diego, 9500 Gilman Drive, La Jolla, California, 92093, United States
[d] Department of Radiology, University of California San Diego, La Jolla, California, 92093, United States
* Email: jjokerst@ucsd.edu

ABSTRACT

Inorganic nanomaterials hold immense potential in theranostics but their translation is limited by the toxicity resulting from non-degradability. Bulk phosphate-based glasses offer great biodegradability, biocompatibility, and easiness in incorporating imaging dyes and drugs. However, the facile and mild solution-based synthesis of micro-/nano particles of this material is yet to be explored. Inspired by the biosilicification process in the diatom, we created PEI/phosphate aggregates via the hydrogen bonding between amine (PEI) and hydroxyl (phosphate) groups, which was proved by dynamic light scattering and ^{1}H nuclear magnetic resonance. The sol-gel reaction between the calcium precursor and PEI/phosphate aggregates yielded degradable polyethylenimine/calcium phosphate (PEI/CP) micro-/nano composites with versatile sizes (396±128 nm to 63±8 μm) and morphologies (hexagonal micro-disc, micro-flower, micro-leaf, nano-butterfly, and nano-ribbon). PEI/CPs composition and chemical structure were examined. PEI/CPs have negligible cell cytotoxicity and degrade within 24 h. In vitro studies showed the promise of PEI/CP in transient ultrasound and photoluminescence imaging.

KEYWORDS

Biodegradation • sol-gel • biomimicking • calcium phosphate • ultrasound imaging

INTRODUCTION

Inorganic nanomaterials hold immense potential in theranostics.[1-11] Specific for bioimaging, inorganic nanomaterials have the advantage of controllable size, chemically functionalizable surfaces, and unique physical properties creating imaging signals. For example, gold nanoparticles are a versatile imaging agent for photoacoustic imaging owing to surface plasmon resonance.[1] Semiconducting quantum dots have tunable emission spectra, photostability, and high efficiency ideal for fluorescent imaging.[12-14] Superparamagnetic iron oxide nanoparticles are good contrast agents for magnetic resonance imaging (MRI).[15-16] Silica nanoparticles have a high acoustic impedance mismatch and can improve ultrasound imaging.[17] Despite these successes, one major limitation of most inorganic nanomaterials is without/slow biodegradability and high toxicity resulted from the long-term retention.[18-22] Therefore, biodegradation into non-toxic and renal clearable components is an ideal property for theranostic nanomaterials.[23-28]

Metal oxide-doped phosphate (MODP) is an emerging class of biomaterial. MODP can be crystalline or non-crystalline. Crystalline MODP nanomaterials, e.g. calcium phosphate (CP) nanocrystals, can be easily prepared from the controlled precipitation of metal ions (e.g. Ca^{2+}) and $H(PO_4)^{2-}$ ions and show promising biomedical applications, e.g. gene delivery to breast cancer with fluorescent imaging.[29-31] However, these CP nanocrystals are not degradable at the physiological pH (~ 7.3), making them still suffer from the long-term retention problem when applied at the physiological pH. Even though they can degrade at more acidic conditions (pH <6), i.e. within the endosome/lysosome (pH 6-4.5), the resulted over-concentrated ions within the cell can trigger the cell necrosis.[31] On the other hand, amorphous MODP, or phosphate-based glasses, are known for excellent biodegradability and biocompatibility at both the physiological and acidic pH values.[32] This degradability is a result of their amorphous structure: the terminal oxygen in the PO_4^{3-} tetrahedron reduces the connectivity of the phosphate network. After degradation, they release ions routinely found in the human body (e.g., PO_4^{3-}, Ca^{2+}, and Na^{+}).[33] Finally, phosphate glasses can be facilely functionalized by incorporating imaging dyes[34] and drugs[35-36]. However, an obstacle to the wide theranostic application of phosphate glasses is the lack of facile, mild, and solution-based methods for preparing this material into monodispersed particles with controllable sizes. Ideally, the size should be tunable from nanometers to microns for customized theranostic tasks. Take ultrasound imaging as an example, the pore size of tumor endothelium constrains the size of contrast agents to less than 380 nm for tumor targeting;[37] Cell labelling requires the contrasts to be sufficiently small for efficient cell uptake.[17] While for the vascular imaging, contrasts of several microns (comparable to blood cells, e.g. microbubbles) are more suitable considering stronger echogenicity.[38-39] Phosphate glass particles (PGP) of 200 nm -3 μm have been prepared via sol-gel combined with electrospray.[34, 40-41] These PGPs show strong echogenicity effective in in-vivo ultrasound imaging and easiness in incorporating dyes for fluorescence imaging. Moreover, their biodegradability and biocompatibility circumvent the long-term toxicity issue.[34] However, this synthetic approach is limited by sophisticated instrumentation, risk of electric shock (20-30 kV), and high temperature (180 °C) incompatible with temperature-sensitive drugs, peptides, and proteins.[40-41]

One may learn from biosilicification in nature to design a solution-based method for preparing phosphate glass micro-/nano particles. Diatoms are unicellular photosynthetic organisms known for the sophisticated design of their silica-based cell walls via the

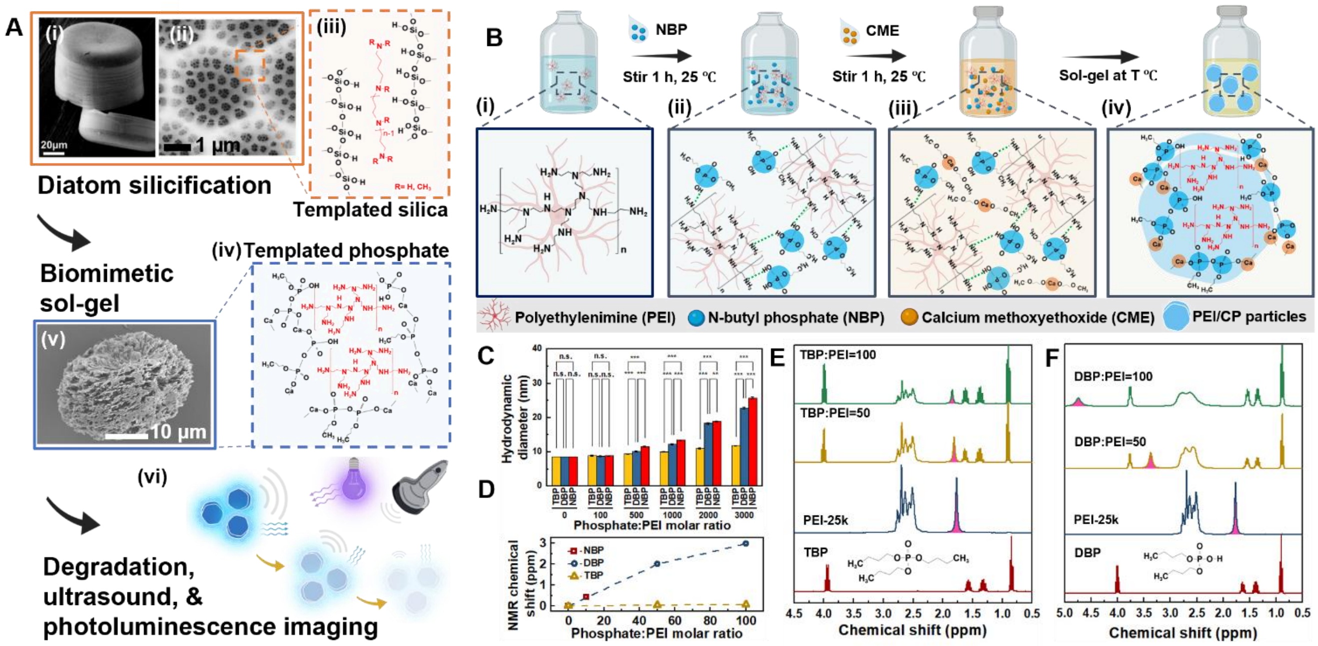

Figure 1. Diatom-inspired synthesis of PEI/CPs for transient ultrasound and photoluminescence imaging. SEM images showing the A(i) diatom cell (Coscinodiscus) and A(ii) silica cell wall made from the A(iii) biosilicification process, where silicic acids are templated by long-chain polyamine via hydrogen bonding between amine and hydroxyl groups and polycondense to form patterned silica.[42] Reproduced from [43], Copyright (2004) Royal Society of Chemistry. A(iv) Scheme showing that mimicking the biosilicification, phosphate precursors can also be templated by PEI and further reaction between phosphate and calcium precursors produces PEI/CPs. A(v) SEM image showing an example of as-prepared PEI/CP structure (PEI/CP-3). A(vi) Scheme showing the biodegradation and decay of the ultrasound and photoluminescence signal of PEI/CPs in water. (B) The synthesis simply adds NBP to B(i) PEI in ethanol to form B(ii) templated PEI/NBP aggregates. These aggregates serve as nuclei in B(iii) the sol-gel reaction between CME and NBP to form B(iv) PEI/CPs particles. (C) Hydrodynamic diameter of PEI/phosphate aggregates versus phosphate:PEI molar ratio as measured by DLS showing that the aggregate size increases only with phosphate esters containing hydroxyl groups (DBP and NBP). ns: not significant, * $p<=0.05$, ** $p<=0.01$, *** $p<=0.001$; n=3. (D) ^{1}H NMR chemical shift of amine versus phosphate:PEI molar ratio showing that the amine peak shifts only with phosphate esters containing hydroxyl groups (DBP and NBP). ^{1}H NMR spectra of PEI-25k (1 mM) and its mixture with (E) TBP and (F) DBP. 300 MHz, $CDCl_3$, 298 K. Amine peak of PEI (1.8 ppm)[44] is filled in pink.

biosilicification process.[5, 42-43, 45] In this process, silicic acids are attracted and templated by amine-rich polypeptides (silaffins) or long-chain polyamines via hydrogen bonding between the hydroxyl and amine groups. The templated silicic acid further poly-condensates to form biosilica.[42, 45] We hypothesized that a similar interaction could happen between phosphate precursors and synthetic polyamines (e.g. polyethylenimine (PEI)), which may be exploited to produce phosphate micro-/nano particles.

Here, we report, for the first time, the synthesis of biodegradable PEI/calcium phosphate (PEI/CP) micro-/nano composites via the biomimetic route for transient ultrasound and photoluminescence imaging. Inspired by the bio-silicification process of diatoms, we applied PEI to template phosphate esters in solution and eventually produced PEI/CP particles with controllable size and morphology at a mild temperature range (25-90 °C). The interaction between phosphate precursors and PEI was systematically studied by dynamic light scattering (DLS) and ^{1}H nuclear magnetic resonance (NMR), confirming the formation of PEI/phosphate aggregates referred to as “phosphate sponges”. These phosphate sponges act as nuclei and mediate the growth of PEI/CP particles. The size, morphology, composition, and chemical structure were characterized using DLS, scanning electron microscopy (SEM), transmission electron microscopy (TEM), optical microscopy, inductively coupled plasma mass spectroscopy (ICP-MS), energy-dispersive X-ray spectroscopy (EDX), Fourier transform infrared spectroscopy (FTIR), X-ray diffraction (XRD), and solid-state ^{31}P and ^{1}H magic angle spinning nuclear magnetic resonance (MAS NMR). Lastly, their biodegradability, cell cytotoxicity, and promise for transient ultrasound and photoluminescence imaging were validated.

RESULTS AND DISCUSSION

Synthetic strategy and mechanism. We hypothesized that the hydroxyl-amine hydrogen bonding between silicic acid and polyamines found in diatom (Figure 1A(i-iii))[42-43] could also form between the phosphate precursor and synthetic PEI. This interaction may result in templated phosphate precursor (Figure 1A(iv)) and be exploited to produce structured PEI/CP micro-/nano composites (Figure 1A(v)). Besides, these PEI/CPs may be degradable in the aqueous environment and used as transient ultrasound and photoluminescence imaging agents (Figure 1A(vi)).

The synthesis (Figure 1B) simply added n-butyl phosphate (NBP) and calcium methoxyethoxide (CME) stepwise to branched PEI in ethanol. Ethanol was used instead of water to avoid the uncontrollable hydrolysis of CME.[32, 46] Then, the sol-gel reaction between NBP and CME was allowed at the controlled stirring rate (0-500 rpm), temperature (25-90 °C), and time (1-18.5 h) (see Methods and Table S1 for detailed parameters). NBP was chosen as the phosphate precursor because of its well-known reactivity with CME.[32] Mixing PEI and NBP may form PEI/NBP aggregates with reactive NBP on the surface via the hydrogen bonding between the hydroxyl group (NBP) and amine group (PEI) (Figure 1B(ii)). We term these aggregates as “phosphate sponge” in analogy to the well-known “proton sponge”.[47] Upon the addition of CME (Figure 1B(iii)), it may react with NBP on phosphate sponges' surface (via hydrolysis and polycondensation) to form PEI/CP micro-/nano composites (Figure 1B(iv)).

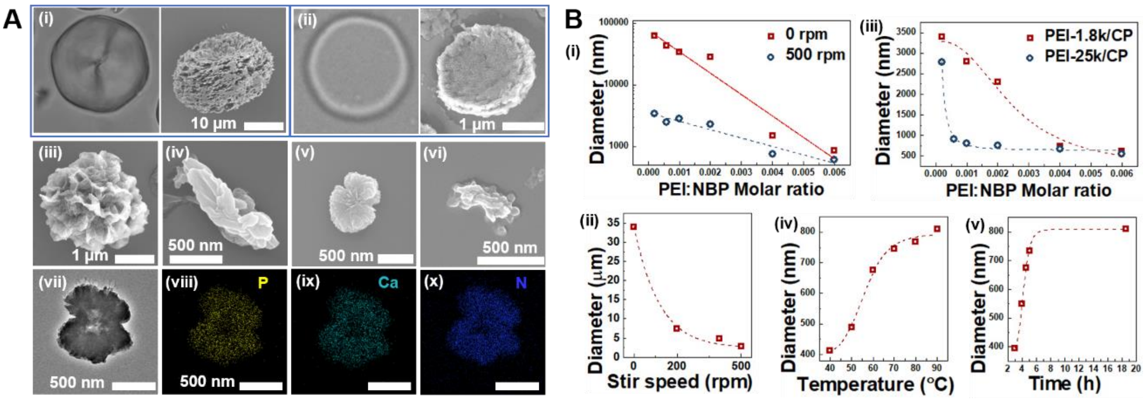

Figure 2. Exemplar particles and effects of synthetic parameters. Optical microscopy and SEM images showing A(i-ii) hexagonal micro-discs (PEI/CP-3 and -10), A(iii) micro-flower (PEI/CP-5), A(iv) micro-leaf (PEI/CP-25), A(v) nano-butterfly (PEI/CP-17), and A(vi) nano-ribbon (PEI/CP-22). A(vii-x) TEM and EDX mapping of the nano-butterfly (PEI/CP-17) showing element P, Ca, and N. The diameter decreases with increasing B(i-ii) PEI:NBP molar ratio, stir speed, and B(iii) PEI molecular weight, while increasing with increasing B(iv) reaction temperature and B(v) time.

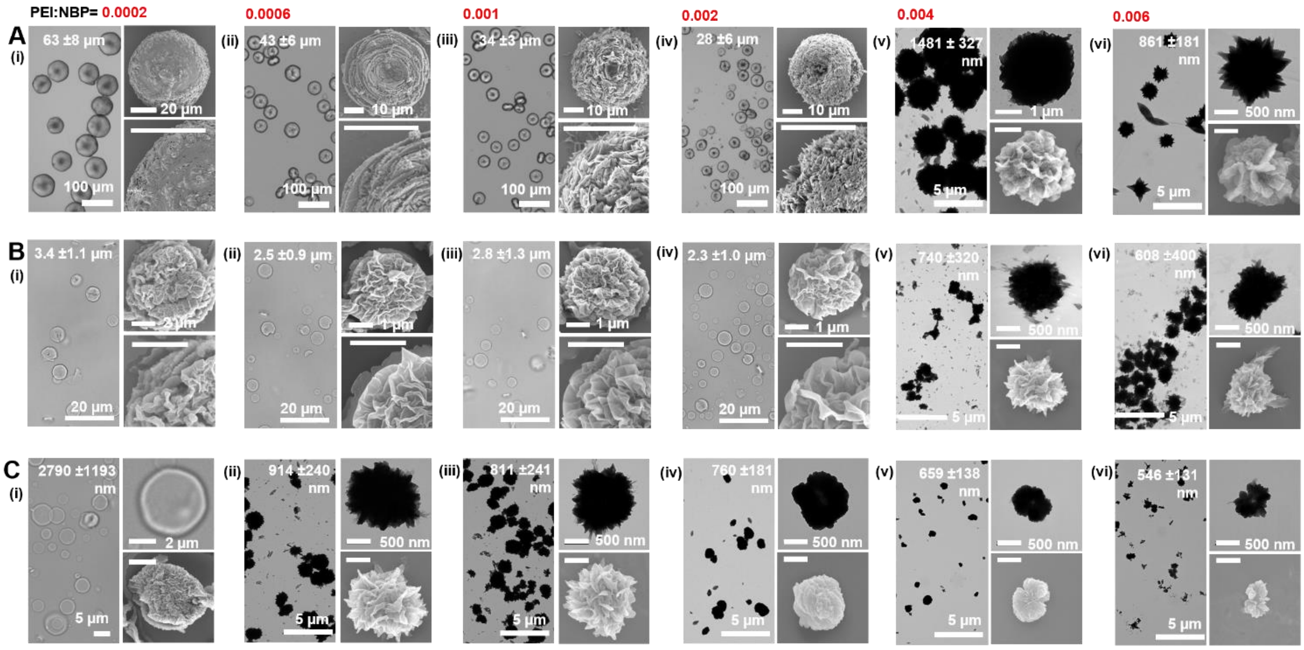

Figure 3. Effects of PEI:NBP molar ratio, magnetic stirring, and PEI molecular weight. Optical microscopy (white, low-magnification), SEM (white, high-magnification), and TEM (black) images of PEI/CPs prepared from (A) PEI-1.8k, 90 °C, 18.5 h, no stirring, and various PEI:NBP molar ratio (PEI/CP-1 to -6), (B) PEI-1.8k, 90 °C, 18.5 h, 500 rpm stirring, and various PEI:NBP molar ratio (PEI/CP-7 to -12), and (C) PEI-25k, 90 °C, 18.5 h, 500 rpm stirring, and various PEI:NBP molar ratio (PEI/CP-13 to -18).

To verify the as-proposed phosphate sponge mechanism, the interaction between phosphate esters and branched PEI of 25k MW was studied using dynamic light scattering (DLS) (Figure 1C and S1) and ^{1}H nuclear magnetic resonance (NMR) (Figure 1D-F and S2). Tri-butyl phosphate (TBP), di-butyl phosphate (DBP), and NBP are phosphate esters with 0, 1, and 1.5 equivalent hydroxyl groups on average (Figure S1A). In DLS measurements, ethanol was used to keep the same solvent condition as the synthesis process. DLS results showed a nearly invariant PEI hydrodynamic diameter (~10 nm) in the presence of increasing TBP (Figure 1C and S1B). While a steady increment of the diameter was observed when increasing the DBP and NBP addition (Figure 1C and S1C-D), indicating the formation of PEI/phosphate aggregates is only possible when the phosphate precursor contains hydroxyl groups. To further prove that the formation of PEI/phosphate aggregates is governed by the hydrogen bonding between hydroxyl and amine groups, the chemical shift of the amine groups (PEI) was tracked by ^{1}H NMR when PEI was titrated by these phosphate esters (Figure 1D-F and S2). $CDCl_3$ was used as the solvent to exclude the hydroxyl groups from the solvent. The amine peak of PEI (1.8 ppm[44], highlighted in pink, Figure 1E) remained invariant despite increasing TBP addition. While in cases of both the DBP and NBP addition, the amine peak shifts steadily towards the downfield direction (Figure 1F and S2). Therefore, both DLS and ^{1}H NMR results support the formation of the phosphate sponge via hydrogen bonding between hydroxyl and amine groups.

Exemplar particles, composition, and chemical structure. This PEI-mediated sol-gel approach is simple (stepwise additions of reactants and incubation) and mild (25 - 90 °C). Moreover, it is highly flexible in controlling PEI/CPs' morphology (Figure 2A) and size (Figure 2B) when parameters were tuned. These parameters include the PEI:NBP molar ratio, solution dynamic condition, PEI molecular weight, reaction temperature, and reaction time (See Table S1 for detailed parameters). The effects of these parameters will be discussed in detail later (Figure 3-4). Briefly, PEI/CP particles ranging from 63±8 μm to 396±128 nm and versatile morphologies were obtained, including hexagonal micro-disc (Figure 2A(i-ii)), micro-flower (Figure 2A(iii)), micro-leaf (Figure 2A(iv)), nano-butterfly (Figure 2A(v)), and nano-ribbon (Figure 2A(vi)).

We expected as-prepared particles to be composites of PEI and calcium phosphate phases. The composite nature was proved using three tools. First, energy-dispersive X-ray (EDX) mapping shows three major elements: P, Ca, and N (Figure 2A(vii-x)). Second, Fourier transform infrared (FTIR) spectra of seven representative PEI/CPs (Figure S3) show characteristic bands of PEI and phosphate species. Specifically, bands of PEI were seen at 2952-2862 and 1453 cm^{-1} (CH_2CH_2), 1620-1585 cm^{-1} (NH), and 1122 cm^{-1} (CN).[48-49] The phosphate phase was evidenced by bands at 1220 cm^{-1} (νas $(PO_2)^-$), 1000 and 1070 cm^{-1} (νas $(PO_3)^{2-}$), 900 cm^{-1} (νs (P-O-P)), and 790, 730, and 540 cm^{-1} (δ (P-O-P)).[46] Lastly, solid-state ^{31}P and ^{1}H magic angle spinning nuclear magnetic resonance (MAS NMR) shows the presence of phosphate species and amine groups (Figure S5 and Table S3). The calculation of the composition based on inductively coupled plasma mass spectroscopy (ICP-MS) (Table S2) showed that the weight percentage of PEI (or calcium phosphate) varies from 67.34 (32.66%) to 50.26 (49.74%), depending on synthetic conditions. Besides, the calcium phosphate phase has a formula of $(P_2O_5)_x(CaO)_{1-x}$ with x varying from 0.31 to 0.40.

X-ray diffraction (XRD) spectra of PEI/CPs (Figure S4) were compared to those of nine typical calcium phosphate (CP) phases reported in the literature[40, 50-57]. The major XRD peaks of PEI/CPs created from PEI-25k match well with those of the HAp crystal[57] but are broader; PEI/CPs prepared from PEI-1.8k have an even broader XRDpattern like the amorphous electrospray CP,[40] indicating the glassy nature of PEI/CPs. Based on the broadness of XRD peaks, the degree of crystallization decreases in the order of HAp > PEI-25k/CP > PEI-1.8k/CP > electrospray CP.

There are three possible bonding types contributing to the PEI/CP network formation: P-O-P bonding, PO-Ca-OP bonding, and/or POH-NH_2 hydrogen bonding. We firstly investigated the nature of P-O-P bonding using solid-state ^{31}P MAS NMR. Q^n is widely applied to represent phosphate species, where n is the number of P-O-P bonding (i.e. bridging oxygens) in each PO_4^{3-} tetrahedron.[32] For PEI/CPs prepared from both PEI-1.8k and -25k, all ^{31}P resonances (Figure S5 and Table S3) were observed between -4 and 4 ppm, which can be assigned to the Q^1 speciation (i.e. pyrophosphates).[58] Therefore, pyrophosphate is the building block of PEI/CPs. Figure S5I shows the chemical structure of pyrophosphate with four isolated oxygens highlighted. Assuming the presence of calcium oxide and partially reacted NBP, each of the four isolated oxygens can form PO-Ca, PO-H, or PO-$CH_2CH_2CH_2CH_3$ groups. Pyrophosphate units containing different combinations of these chemical groups are different Q^1 species measurable by ^{31}P MAS NMR (Figure S5). We observed only one dominant Q^1 peak (~1ppm) in all PEI-25k/CPs (Figure S5D-H) and those prepared from a high PEI-1.8k concentration (Figure S5C). Pyrophosphate units in these PEI/CPs are mainly connected by PO-Ca-OP because their ICP-MS-measured composition (Table S2) is close to $(P_2O_5)_{0.33}(CaO)_{0.67}$, which is the theoretical composition of the Q^1 speciation saturated by Ca. In contrast, multiple Q^1 species were seen from PEI/CPs prepared from low PEI-1.8k concentrations (Figure S5A-B). Besides, the ICP-MS-measured P_2O_5 ratio of these particles is larger than 0.33. Both results support the presence of PO-H and/or PO-$CH_2CH_2CH_2CH_3$ along with PO-Ca. PO-H may form hydrogen bonding with NH_2 (PEI) and therefore, further connects pyrophosphate units and extends the network. Indeed, ^{1}H MAS NMR results (Figure S5A-B) of PEI/CPs containing multiple Q^1 species also show multiple amine peaks including those highly shifted (>9 ppm), which supports the formation of POH-NH_2 hydrogen bonding.

Effects of PEI:NBP molar ratio. Sol-gel reactions were firstly performed using PEI-1.8k at 90 °C for 18.5 h without magnetic stirring. The PEI:NBP molar ratio was varied from 0.0002 to 0.006. The average diameter of PEI/CPs decreases as the molar ratio increases and can be tuned from 63±8 μm (ratio=0.0002) to 861 nm (ratio=0.006) (Figure 2B(i) and 3A. See Figure S6 for size distributions.). PEI/CPs appeared to be porous hexagonal micro-discs with the size ranging from 28±6 to 63±8 μm when the molar ratio was between 0.0002 and 0.002 (Figure 2A(i) and 3A(i-iv)). High-magnification SEM images (Figure 3A(i-iv)) indicate that these hexagonal micro-discs may be assembled from smaller micro-flakes, which is supported by particle growth studies shown later (Figure 4B). This PEI:NBP molar ratio-dependent size change can be explained by the proposed phosphate sponge mechanism. Phosphate sponges can be considered as nuclei for particle growth. With a fixed NBP and CME addition, a higher PEI:NBP molar ratio results in a higher number-concentration of nuclei and, therefore, smaller particles.

Effects of solution dynamic condition. We then repeated sol-gel reactions using PEI-1.8k at 90 °C for 18.5 h with magnetic stirring at 500 rpm. At the same PEI:NBP molar ratio, magnetic stirring at 500 rpm resulted in 18.5 to 1.4 times smaller particles than no stirring (Figure 2B(i)). These particles also appeared to be micro-discs with the molar ratio ranging from 0.0002 to 0.002 (Figure 3B(i-iv)) and micro-/nano flowers when the ratio was above 0.002 (Figure 3B(v-vi)). By carefully controlling the stirring speed from 0 to 200, 400, and 500 rpm, the average particle size can be finely tuned from 34±3 to 7.8±2.7, 4.8±1.4, and 2.8±1.3 μm (Figure S6C and S7).

Effects of PEI molecular weight. To determine the influences of the PEI molecular weight, PEI-1.8k was replaced by either PEI-25k or PEI-800 while other conditions were kept the same (Figure 3C). Comparing Figure 3C to Figure 3B, at the same PEI:NBP molar ratio, PEI-25k resulted in smaller particles. This trend is clearer in Figure 2B(iii). The micro-disc shape (~2790 nm) appeared when the molar ratio was 0.0002 (Figure 3C(i)). When the molar ratio exceeded 0.0002, submicron-flowers (914±240 to 760±181 nm) and nano-butterflies (659±138 to 546±131 nm) were formed (Figure 3C(ii-vi)). The PEI molecular weight-dependent size change can be explained by the difference in chemical bonding. Based on the solid-state ^{31}P and ^{1}H MAS NMR results discussed before (Figure S5 and Table S3), PEI/CPs prepared from low-concentration PEI-1.8k can extend their network via both PO-Ca-OP and POH-NH_2 hydrogen bonding, which explains for larger particles formed in these conditions. However, in the case of high-concentration PEI-1.8k and PEI-25k, the connection of pyrophosphate units via the POH-NH_2 hydrogen bonding is less likely, resulting in smaller particles. As shown in Figure S8, within the tested range of PEI:NBP molar ratio (0.0002 to 0.006), PEI-800 did not produce monodispersed particles with defined shapes as seen in the case of PEI-1.8 and PEI-25k. Instead, only amorphous gel-like products were observed. This difference indicates that PEI-800 may be too small to efficiently regulate the growth of monodispersed PEI/CP particles.

Effects of reaction temperature. Sol-gel reactions were also carried out at various temperatures (90, 80, 70, 60, 50, and 40 °C) with other parameters being kept constant (PEI-25k:NBP=0.001, magnetic stirring at 500 rpm, and 18.5 h). The average diameter of particles increased as the reaction temperature was raised (Figure 2B(iv) and 4A). At 40 and 50 °C, particles have a nano-ribbon morphology (490 and 412 nm) (Figure 4A(i-ii)). When the temperature was adjusted between 60 °C and 90 °C, particles possess the nano-flower morphology (from 811±241 to 768 ±148, 746±171, and 677±134 nm) (Figure 4A(iii-iv)). The temperature-dependent change of particle size can be explained by the reaction kinetics. A higher reaction temperature may result in faster reaction and particle growth and therefore, a larger size during a given period of reaction.

Effects of reaction time. Hexagonal micro-disc (PEI/CP-3) and nano-flower (PEI/CP-15) were chosen as models to understand the growth of PEI/CP particles. Particles were collected at different time points and examined. Figure 4B shows the evolution of the hexagonal micro-disc (PEI/CP-3) over time. The first hour of reaction at room temperature resulted in an inhomogeneous mixture of nano-spheres (~80 nm) and nano-rods (LxW=400x150 nm, Figure 4B(i)). After raising the

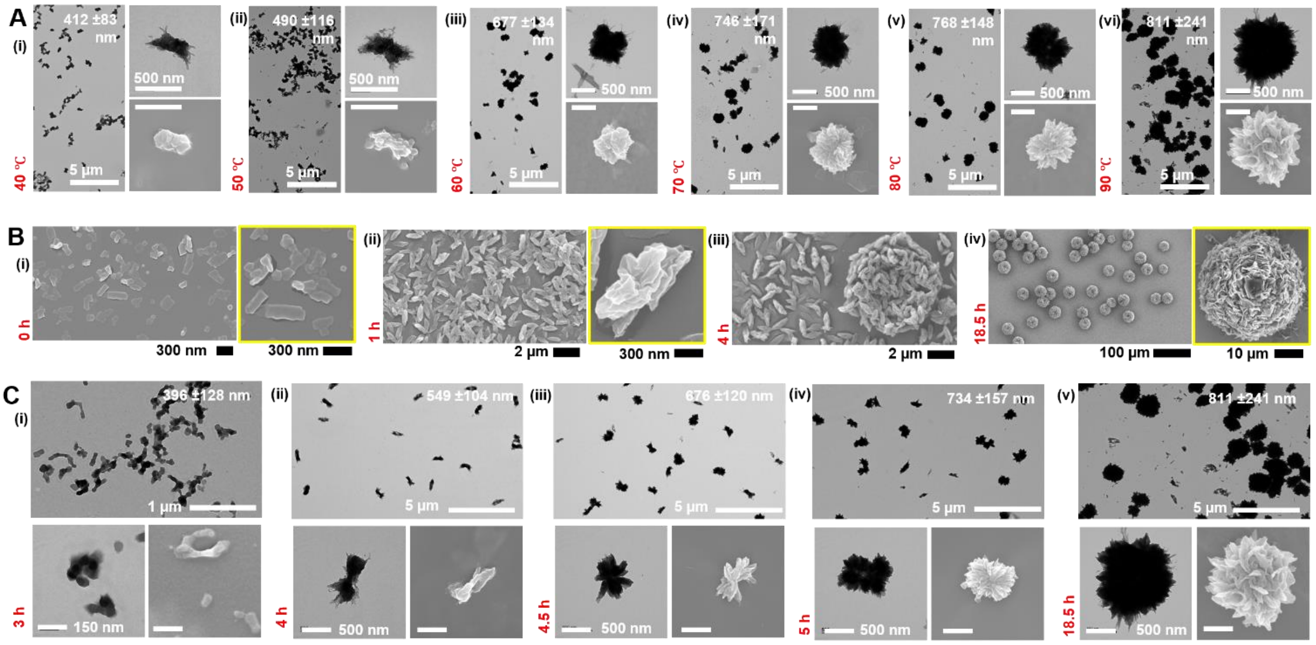

Figure 4. Effects of reaction temperature and time. SEM (white) and TEM (black) images of PEI/CPs prepared from (A) PEI-25k, PEI:NBP molar ratio 0.001, 90 °C, 18.5 h, 500 rpm stirring, and various temperature: A(i) 40 °C (PEI/CP-23), A(ii) 50 °C (PEI/CP-22), A(iii) 60 °C (PEI/CP-21), A(iv) 70 °C (PEI/CP-20), A(v) 80 °C (PEI/CP-19), and A(vi) 90 °C (PEI/CP-15). Growth process of (B) hexagonal micro-disc (PEI/CP-3) and (C) nano-flower (PEI/CP-15).

temperature to 90 °C for another hour, these mixed structures transformed into homogenous micro-leaves (LxW=1200x400 nm, Figure 4B(ii)). When extending the reaction time at 90 °C to 4 h (Figure 4B(iii)), the size and shape of micro-leaves remained almost the same; Meanwhile, parts of these micro-leaves assembled to form a loose micro-disk structure (~7 μm in diameter), implying the transition from micro-leaves' growth to the assembly during this period. Finally, when the reaction time at 90 °C reached 18.5 h, micro-leaves disappeared, and larger and homogeneous hexagonal micro-discs (34±3 μm in diameter) were observed (Figure 4B(iv))). In short, the formation of hexagonal micro-discs started with the growth of micro-leaves from a mixture of nano-spheres and nano-rods. As-formed micro-leaves then assembled to form the loose micro-disc structure. Finally, further deposition of materials on the micro-disc surface led to the formation of larger and denser hexagonal micro-discs.

A similar observation was performed for nano-flowers (PEI/CP-15, Figure 4C). The growth of PEI/CP-15 also began with a mixture of nano-spheres and nano-rods with an average diameter of 396±128 nm (3 h at 90 °C, Figure 4C(i)). After 4 h at 90 °C, these mixed particles transformed into homogenous nano-ribbons (549±104 nm, Figure 4C(ii)). These nano-ribbons then evolved to nano-flowers with the size increasing from 676±120 nm (4.5 h at 90 °C, Figure 4C(iii)) to 734±157 nm (5 h at 90 °C, Figure 4C(iv)) and 811±241 nm (18.5 h at 90 °C, Figure 4C(v)) (See Figure 2B(v) for the diameter versus time relationship).

Ultrasound and photoluminescence imaging. We hypothesized that PEI/CP particles can have a high acoustic impedance mismatch with the liquid phase and be used as ultrasound contrasts. To determine how the particle size and concentration affects the echogenicity, PEI/CPs in ethanol solution were added to tubes (Figure 5A(i)) and imaged in the B-mode at 18 MHz. Ethanol was used as the solvent at this step to prevent any uncertainties from the degradation caused by water. No ultrasound signal was detected from pure ethanol (Figure 5A(ii)). At the same particle mass concentration (2.5 mg/mL), the ultrasound intensity increases with increasing particle size (546±131 nm to 34±3 μm, Figure 5A(iii)), which is consistent with previous findings and can be attributed to the differences in the scattering cross-section.[59-60] This size effect holds true for all concentrations tested (0-10 mg/mL, Figure 5A(iv)). With a given size, the ultrasound signal increases as the mass concentration increases (Figure 5A(iv)). A linear intensity-concentration relationship was seen at the lower concentration range (Figure S9). Defining the limit of detection (LOD) as the concentration of particles creating the intensity at three standard deviations above the mean of the background and using the background value of 0.08±0.01 and the best-fit equations (Figure S8), we estimated the LOD of PEI/CPs of 34±3 μm, 7.8±2.7 μm, 4.8±1.4 μm, and 546±131 nm to be 0.17, 0.30, 1.47, and 11.10 μg/mL, respectively. The LOD of 546±131 nm PEI/CP is comparable with that reported for silica NPs (18.5 μg/mL, 300 nm, at 16 MHz), which has been demonstrated feasible for in-vivo stem cell imaging.[17]

Contrasts with size comparable to blood cells have been used for Doppler vascular imaging.[38-39] Here, we tested in vitro the potential of using PEI/CPs for Doppler imaging. As a negative control, pure ethanol was constantly pumped through a channel inside an agarose phantom using a peristaltic pump, which did not result in detectable color-Doppler signals (Figure 5B(i)). In contrast, flowing 10 mg/mL PEI/CP-31 (7.8 μm) generated color-Doppler signals with recognizable flow directions (red or blue, Figure 5B(ii-iii). The power-Doppler mode is used clinically to monitor heartbeats and changes in blood flow rate. Taking the advantage of the pulsive flow of the peristaltic pump, we were able to mimic the heartbeat. Heartbeat-like wavy power-Doppler signals were observed from the flow of PEI/CP-31 but not ethanol or stagnant particles (Figure 5C).

PEI/CPs also emitted blue light when excited at 358 nm (Figure 5D(i)). This is due to the intrinsic photoluminescence of PEI reported previously, although the mechanism of this intrinsic photoluminescence is yet to be explored.[61] The emission peak of pure PEI-1.8k and PEI/CPs were found at 411 nm and 450 nm (excitation at 350 nm, Figure S10).

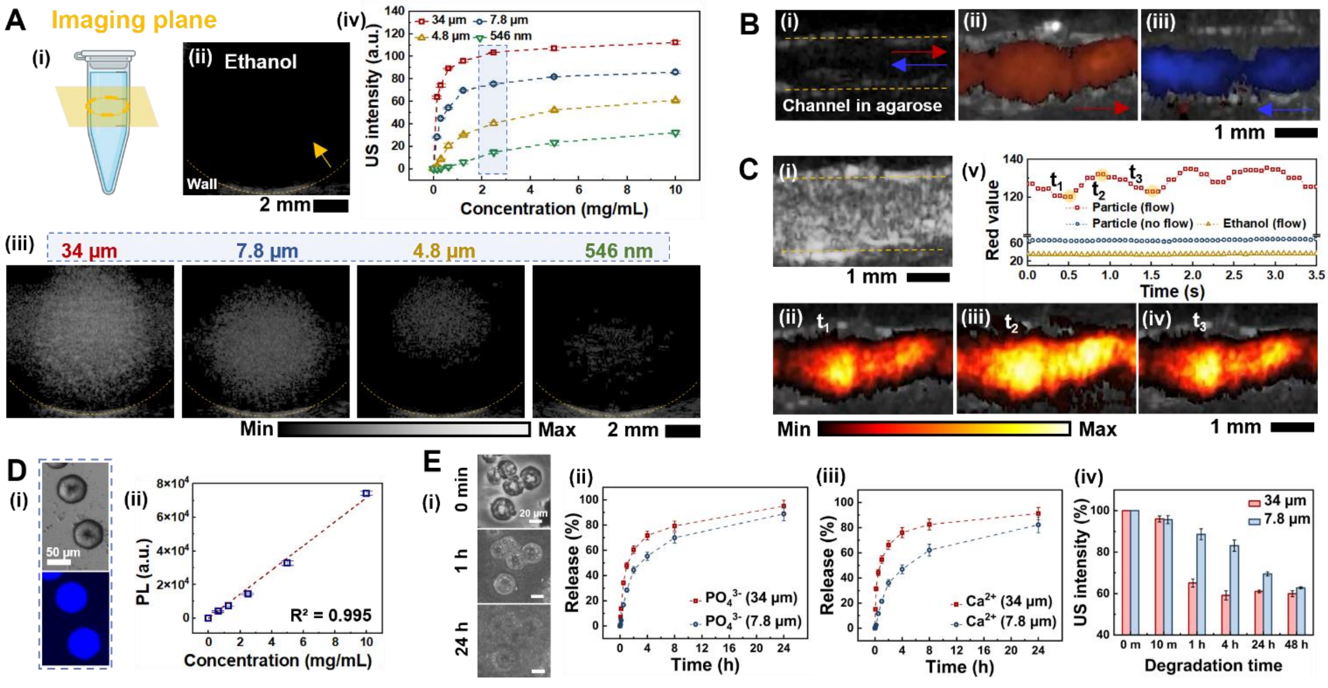

Figure 5. Ultrasound and photoluminescence imaging and biodegradability. (A) B-mode imaging. A(i) Imaging slice in a tube. B-mode images of A(ii) ethanol and A(iii) 2.5 mg/mL ethanol solution of PEI/CP-3 (34 ± 3 μm), PEI/CP-31 (7.8 ± 2.7 μm), PEI/CP-32 (4.8 ± 1.4 μm), and PEI/CP-18 (546 ± 131 nm). Dashed lines and arrow show the tube wall. A(v) Ultrasound intensity versus particle concentration. (B-C) Doppler imaging. Overlay of color Doppler and B-mode images when flowing B(i) water and B(ii-iii) 10 mg/mL PEI/CP-31 (7.8 ± 2.7 μm) in ethanol. Overlay of power Doppler and B-mode images of 10 mg/mL PEI/CP-31 (7.8 ± 2.7 μm) in ethanol C(i) without and C(ii-iv) with flow at time points marked in C(v). C(v) Doppler intensity versus time. (D) Photoluminescence imaging. D(i) Fluorescence microscopy images showing PEI/CP-3 emitting blue light (DAPI, excitation at 358 nm). D(ii) Photoluminescence intensity versus PEI/CP-3 concentration (excitation at 350 nm). (E) Biodegradability. E(i) Optical microscopy images showing the dissolution of PEI/CP-3 under a continuous flow of PBS. E(ii)-(iii) Release of PO_4^{3-} and Ca^{2+} from PEI/CP-3 under a continuous flow of fresh water (pH 7.30). E(iv) Decay of the ultrasound intensity when PEI/CP-3 and -31 degrade (2.5 mg/mL in 1:1 ethanol and PBS buffer).

The photoluminescence intensity increases linearly with PEI/CPs concentration (Figure 5D(ii)). Although, considering the low quantum yield (1%) reported for PEI-1.8K and PEI-25k,[61] PEI/CPs may not be the best choice of fluorophores, this intrinsic photoluminescence can still be used for labelling and tracking these particles when necessary.

Degradability. The poor clearance of nanomaterials is a major impediment to clinical translation. By design, PEI/CPs should slowly degrade into small molecules and simple ions for renal clearance. We further tested the degradability of PEI/CPs. Optical microscopy images show that PEI/CPs gradually dissolved in PBS buffer (Figure 5E(i)). PEI/CPs were continuously hydrated by fresh water (pH 7.30) and a release of about 80% - 90% major ions (i.e., PO_4^{3-} and Ca^{2+}) were detected within the first 24 h using ICP-MS (Figure 5E(ii-iii)). When dissolving PEI/CPs in a static PBS buffer, the ultrasound intensity dropped about 40% within the first 24 h and only slightly in the next 24 h (Figure 5E(iv)). Therefore, in practice, PEI/CPs can be dispersed in PBS buffer and used as transient ultrasound contrast agents with a 24 h imaging window. They may bridge the gap between the unstable gas microbubbles (degrade within 30 min) 17 and slowly-degradable silica nanoparticles (degrade after 24 days)[62] considering the degradation speed.

Cell cytotoxicity. The dose-dependent cytotoxicity of pure PEIs and PEI/CP composites was evaluated with HEK 293T and HeLa cells using the resazurin assay (Figure 6). Pure PEI-25k showed high cytotoxicity; a low dose of 0.028 mg/mL can dramatically reduce the cell viability to below 20%. PEI-1.8k is less toxic but still caused a steady drop in the viability of HEK 293T (Figure 6A). Surprisingly, PEI/CPs have negligible cytotoxicity compared to PEIs. Both cell types treated with fresh and degraded PEI-25k/CP and PEI-1.8k/CP have viability above 85% in the concentration range tested except HeLa cells treated with 0.909 mg/mL degraded PEI-25k/CPs (77%). In the case of HEK 293T cells, fresh PEI-25k/CP and PEI-1.8k/CP, respectively, resulted in 9-26 and 1-4 times, respectively, higher viability than corresponding PEI; these values are 6-23 and 1-1.6 in the case of HeLa cells (Figure 6C-D).

The toxicity of pure PEI is originated from the damage of the cell membrane by abundant positive amine groups.[63] Therefore, the reduced cytotoxicity of PEI/CPs compared to pure PEI can be explained by the charge neutralization by negative phosphate species in both intact and degraded phases.

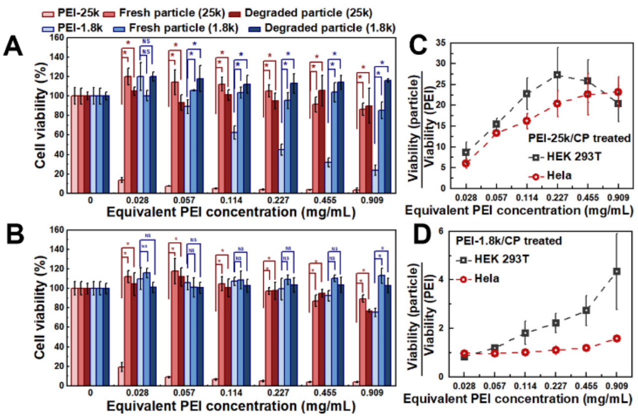

Figure 6. Cell cytotoxicity of pristine PEI and PEI/CPs. Tests used resazurin assay on (A) HEK 293T and (B) HeLa cells. Ratio of cell viability treated with fresh particles to pristine PEI in the case of (C) PEI-25k and (D) PEI-1.8k. PEI/CP-5 was selected to represent particles made from PEI-1.8k and PEI/CP-15 for PEI-25k. PEI/CPs show negligible cytotoxicity compared to pristine PEI. *: P≤0.05; NS: not significant, i.e. p>0.05; n=4.

CONCLUSIONS

We demonstrated a facile and mild (25-90 °C) synthesis mimicking the bio-silicification in diatoms for preparing PEI/CP composites. Using DLS and ^1H NMR, we proved the formation of proposed "phosphate sponges", which are aggregates composed of phosphate esters and PEI resulting from hydrogen bonding between hydroxyl (from phosphate ester) and amine groups (from PEI). These phosphate sponges served as nuclei in the reaction of CME and phosphate esters. By controlling parameters such as the PEI:NBP molar ratio, solution dynamic condition, PEI molecular weight, reaction temperature, and reaction time, PEI/CP composites were prepared with versatile sizes (396±128 nm to 63±8 μm) and morphologies (hexagonal micro-disc, micro-flower, micro-leaf, nano-butterfly, and nano-ribbon). PEI/CPs exhibited excellent biocompatibility and biodegradability, indicated by negligible cell cytotoxicity and degradation within 24 h. The echogenicity of PEI/CPs increases with the increment of size and concentration. PEI/CPs also generated Doppler signals containing the flow direction and speed information. Finally, PEI/CPs showed intrinsic blue photoluminescence. We envision that PEI/CPs are promising transient ultrasound and photoluminescence imaging agents.

METHODS

Materials. Ethanol (200 proof, Koptec) and phosphate buffered saline (PBS, x1, Corning) were purchased from VWR. Tri-n-butyl phosphate (TBP, 98%) and branched polyethylenimine (b-PEI, 1.8k MW) were purchased from Alfa Aesar. n-Butyl phosphate (NBP, a 1:1 mixture of mono-n-butyl and di-n-butyl) were purchased from Thermo Scientific. Dibutyl phosphate (DBP, 97.0%), branched polyethylenimine (b-PEI, 25k and 800 MW), chloroform-d ($CDCl_3$, 99.8 atom %D), and resazurin were purchased from Sigma-Aldrich. Calcium methoxyethoxide (CME, 20% in methoxyethanol) was purchased from ABCR Chemical. Ultrapure Agarose (Invitrogen) was purchased from Fisher Scientific.

Synthesis of PEI/CPs. Ethanol was used instead of water to avoid the uncontrollable hydrolysis of CME.[32, 46] Branched PEI (MW 1.8 k or 25k) was dissolved in ethanol to make a $1x10^{-5}$ mol/mL PEI stock solution. An appropriate amount of PEI stock solution was then diluted by extra ethanol to make a desired final PEI concentration. Under magnetic stirring at 500 rpm, NBP was added to the diluted PEI in ethanol. After stirring at room temperature for 1 h, CME was added, and the solution allowed for another 1 h stirring at room temperature. Then, the well mixed solution was incubated at a raised temperature with or without magnetic stirring for a certain reaction time. All detailed parameters including reagents addition, stir speed, temperature, and reaction time can be found in Table S1. As-prepared particles were purified by repeating centrifugation (5000 rpm, 20 min) and ethanol wash for 3 times.

^{1}H NMR and DLS study of the interaction between PEI and phosphate esters. The interaction between PEI and phosphate esters was studied with the combination of liquid state ^{1}H NMR and DLS. PEI (25k MW) was firstly dissolved in either $CDCl_3$ (for liquid state ^{1}H NMR) or ethanol (DLS) to make 1mM PEI solutions. Then an appropriate amount of phosphate precursors (TBP, NBP, or DBP) were mixed with the PEI solution to make desired phosphate:b-PEI molar ratios. ^{1}H NMR spectra were recorded on a Bruker 300 MHz spectrometer and all chemical shifts are referenced to the reported literature[64] ($CDCl_3$: 7.26 ppm). DLS measurements were performed on a Malvern NANO-ZS90 Zetasizer to determine hydrodynamic sizes of PEI/phosphate ester aggregates.

Morphology and size of PEI/CPs particles. SEM images were obtained using Zeiss Sigma 500 operated at 5 kV with a 30-μm aperture and 10 mm working distance. Particles in ethanol were drop-coated on a silicon substrate (Ted Pella Inc.), dried at room temperature, and sputter-coated with gold alloys before SEM. TEM images and EDX mapping were acquired using an FEI Tecnai F20 instrument at an operation voltage of 200 kV. Particles in ethanol were drop-coated on a copper TEM grid and ethanol was evaporated naturally at room temperature before TEM imaging. Keyence fluorescent microscope was used for observations of microparticles either in bright field mode or fluorescence mode (DAPI channel, excitation 358 nm). For characterizing the morphology, ethanol was used as the solvent. To monitor the particle degradation, particles were deposited in a flow cell[65] and PBS was flowed at 1.2 mL/min to simulate the human blood flow. See Figure S11 (Supporting Information) for details of the flow cell design. DLS measurements were performed on a Malvern NANO-ZS90 Zetasizer to determine hydrodynamic sizes of both PEI/phosphate ester aggregates and PEI/CP particles (<1.5 μm) dissolved in ethanol. The size distribution of PEI/CP particles larger than 1.5 μm was determined by image analysis over 500 particles using Image-Pro Plus software based on optical microscopy images.

Spectral studies of the PEI/CPs particles. PEI/CPs in ethanol were dried under vacuum at room temperature and used for spectral studies. FTIR spectroscopy was performed on a Perkin Elmer Spectrum Two FTIR Spectrometer. XRD was performed on Rigaku MiniFlex with Cu Kα radiation (λ = 1.5406 Å). Solid state ^{31}P and ^{1}H MAS NMR. All ^{31}P MAS NMR measurements were performed at 9.4 T using a Bruker 400 MHz Avance III HD spectrometer operating at Larmor frequency of 161.9 MHz (400 MHz for ^{1}H). Samples were loaded under a N_2 atmosphere into Bruker 3.2 mm rotors and spun at a magic angle spinning (MAS) frequency of 15 kHz. Each spectrum was acquired at room temperature by direct excitation (single pulse) methods employing $\pi/4$ pulses of length 2 μs and 80 kHz of ^{1}H decoupling which was applied during data (FID) acquisition. To ensure quantitative results a recycle delay of 300 s was used which were checked against tests of longer recycle delays. All data were referenced against the IUPAC recommended primary reference of 85% H_3PO_4 (δiso= 0.0 ppm), via a secondary solid reference of ammonia dihydrogen phosphate ($(NH_3)H_2PO_4$ or ADP) (δiso = 0.99 ppm). The corresponding ^{1}H MAS NMR room temperature measurements were undertaken at 16.4 T using a Bruker 700 MHz Avance III HD spectrometer operating at a Larmor frequency of 700.13 MHz. All samples were packed under a N_2 atmosphere into Bruker 1.3 mm rotors and spun at a MAS frequency of 60 kHz. To obtain quantitative spectra, direct excitation (single pulse) methods using $\pi/4$ pulses of length 1.25 μs were used in conjunction with a recycle delay of 10 s. All data were referenced against the IUPAC recommended primary reference of tetramethylsilane ($(CH_3)_4Si$ or TMS) (δiso= 0.0 ppm), via a secondary solid reference using the methyl (CH_3) group resonance from alanine (δiso = 1.1 ppm). The acquisition and processing of all SSNMR data was performed using the Bruker TopSpin software package, while deconvolution of spectra was performed using DMFit. Photoluminescence emission measurements were performed on an BioTek Synergy H1 microplate reader.

ICP-MS measurements. ICP-MS measurements were carried out using iCAP RQ, Thermo Scientific. For ICP-MS analysis of particles' composition, overnight digestion of particles was carried out by adding 571 μL 70% Nitric acid to 0.01 mg dried particles in a glass vial. This solution was transferred to a 15mL plastic centrifugation tube and Millipore water was added to make a final solution of 10 mL. For ICP-MS analysis of particles' ion releases, 0.1 mL of 10 mg/mL particle in ethanol was deposited on a syringe filter (Millex-GP, 220 nm). Millipore water (pH 7.30) was continuously pumped (1.2 mL/h) through the particle-loaded syringe filter. The solution was collected at the time points of 0, 5, 10, 30, 60, 120, 240, 480, and 1440 min. Collected solutions were diluted 100 times with 4% HNO3 and measured by ICP-MS.

In vitro ultrasound imaging. Ultrasound images were captured with Verasonics, Vantage 256 system performed at 40 V with a L22-14vX transducer (18 MHz, 3k PRF, 6 pulse cycle, ~30% bandwidth, 128 elements, and 0.10 mm pitch). Ethanol solutions of PEI/CP-3 (34 ± 3 μm), PEI/CP-31 (7.8 ± 2.7 μm), PEI/CP-32 (4.8 ± 1.4 μm), and PEI/CP-18 (546 ± 131 nm) from 0 to 10 mg/mL were loaded into a 1.5 mL plastic centrifuge tube. The tube was immersed in a water bath and B-mode ultrasound images were acquired. To determine the ultrasound intensity decay during the particle dissolution, PEI/CP-3 (34 μm) and PEI/CP-31 (7.8 μm) were dispersed in 1:1 ethanol and PBS buffer solution with a final concentration of 2.5 mg/mL were used. The ultrasound intensity was then quantified by measuring the average RGB value of the same area of interest using Image J. For Doppler imaging, 10 mg/mL PEI/CP-31 (7.8 μm) in ethanol solution was pumped through a channel inside an agarose phantom (2 wt%) with a peristaltic pump. The average red value inside an area of interest was measured using Image J to quantify the power Doppler intensity.

Cell cytotoxicity. The cytotoxicity of materials (pure PEI-1.8k, pure PEI-25k, fresh PEI/CP-5 and -15, and PEI/CP-5 and -15 degraded for 24 hours in PBS) were studied on both HEK 293T and HeLa cells using resazurin assay. 0.1 mL cell solution (200000 count/mL in DMEM with 10% FBS and 1% PS) were loaded to a 96-well plate and incubated for 24 hours (5% CO^2 at 37 °C). 0.01 mL materials in PBS buffer were added to wells containing cells in DMEM to make the final equivalent PEI concentration in the well in the range from 0 to 1 mg/mL. After materials addition, the cells were incubated for another 24 hours (5% CO^2 at 37 °C). 0.01 mL resazurin was then added to each well. After incubation for another 2 hours, the fluorescence was read. A well with only DMEM and resazurin dyes and another well with only cells, DMEM, and resazurin dyes were also prepared following the same volume and incubation condition.

In the case of PEI/CP particles, the equivalent PEI concentration is defined as the resulting PEI concentration assuming a complete dissolution of PEI/CP particles. Therefore, to achieve the equivalent PEI concentration, higher PEI/CP mass concentration was used than pure PEI. The cell viability was calculated as follows:

$$\text{Cell viability} = \frac{\text{FL}_{\text{material}} - \text{FL}_{\text{empty}}}{\text{FL}_{\text{cell}} - \text{FL}_{\text{empty}}} \times 100\%$$

$FL_{material}$: fluorescence intensity read from the well with cells, DMEM, resazurin dyes, and materials (PEI-1.8k, PEI-25k, fresh PEI/CPs, or PEI/CPs degraded for 24 hours); FL_{empty}: fluorescence intensity read from the well with only DMEM and resazurin dyes; FL_{cell}: fluorescence intensity read from the well with only cells, DMEM, and resazurin dyes.

ASSOCIATED CONTENT

Supporting Information

The Supporting Information is available free of charge at Xxxxxx

Synthetic parameters, composition (ICP-MS), DLS and ^{1}H NMR titration showing the formation of PEI/phosphate aggregates, FTIR, XRD, solid state ^{31}P and ^{1}H MAS NMR, size distribution of PEI/CPs particles, schematic illustration of the flow cell design for studying the degradability of particles, optical microscopy images, US intensity versus concentration, and photoluminescence emission spectra.

AUTHOR INFORMATION

Author Contributions

T.H. and J.V.J. conceived the idea. T.H. conducted the major material synthesis. All authors performed the general measurements. T.H. and J.V.J. drafted the manuscript. All authors discussed the results and commented on the manuscript.

Notes

The authors declare no competing financial interest.

ACKNOWLEDGMENTS

The authors acknowledge the support from the NSF funding under award 1845683 and NIH funding under award P30 NS047101. This work was performed in part at the San Diego Nanotechnology Infrastructure (SDNI) of University of California San Diego, a member of the National Nanotechnology Coordinated Infrastructure (NNCI), which is supported by the National Science Foundation (Grant ECCS-1542148). The authors acknowledge the use of facilities and instrumentation supported by NSF through the UC San Diego Materials Research Science and Engineering Center (UCSD MRSEC) (Grant DMR-2011924). M. X. acknowledge the support from NIH funding (R21 AI157957). S.-T.K. and J.L. acknowledge partial support from the NSF MRSEC program through the UC Irvine Center for Complex and Active Materials (DMR-2011967). J.V.H. acknowledges financial support for the solid state NMR instrumentation at Warwick used in this research which was funded by the EPSRC (grants EP/M028186/1 and EP/K024418/1), the BBSRC, the University of Warwick, and the Birmingham Science City AM1 and AM2 projects which were supported by Advantage West Midlands (AWM) and the European Regional Development Fund (ERDF).

REFERENCES

(1) Weber, J.; Beard, P. C.; Bohndiek, S. E., Contrast agents for molecular photoacoustic imaging. *Nature Methods* **2016,** *13* (8), 639-650.

(2) Liu, H.; Hu, Y.; Sun, Y.; Wan, C.; Zhang, Z.; Dai, X.; Lin, Z.; He, Q.; Yang, Z.; Huang, P.; Xiong, Y.; Cao, J.; Chen, X.; Chen, Q.; Lovell, J. F.; Xu, Z.; Jin, H.; Yang, K., Co-delivery of Bee Venom Melittin and a Photosensitizer with an Organic–Inorganic Hybrid Nanocarrier for Photodynamic Therapy and Immunotherapy. *ACS Nano* **2019,** *13* (11), 12638-12652.

(3) Guo, J.; Agola, J. O.; Serda, R.; Franco, S.; Lei, Q.; Wang, L.; Minster, J.; Croissant, J. G.; Butler, K. S.; Zhu, W.; Brinker, C. J., Biomimetic Rebuilding of Multifunctional Red Blood Cells: Modular Design Using Functional Components. *ACS Nano* **2020,** *14* (7), 7847-7859.

(4) Cao, J.; Zaremba, O. T.; Lei, Q.; Ploetz, E.; Wuttke, S.; Zhu, W., Artificial Bioaugmentation of Biomacromolecules and Living Organisms for Biomedical Applications. *ACS Nano* **2021,** *15* (3), 3900-3926.

(5) Guo, J.; Amini, S.; Lei, Q.; Ping, Y.; Agola, J. O.; Wang, L.; Zhou, L.; Cao, J.; Franco, S.; Noureddine, A.; Miserez, A.; Zhu, W.; Brinker, C. J., Robust and Long-Term Cellular Protein and Enzymatic Activity Preservation in Biomineralized Mammalian Cells. *ACS Nano* **2022,** *16* (2), 2164-2175.

(6) Wang, Y.; Du, W.; Zhang, T.; Zhu, Y.; Ni, Y.; Wang, C.; Sierra Raya, F. M.; Zou, L.; Wang, L.; Liang, G., A Self-Evaluating Photothermal Therapeutic Nanoparticle. *ACS Nano* **2020,** *14* (8), 9585-9593.

(7) Chen, J.; Ma, Y.; Du, W.; Dai, T.; Wang, Y.; Jiang, W.; Wan, Y.; Wang, Y.; Liang, G.; Wang, G., Furin-Instructed Intracellular Gold Nanoparticle Aggregation for Tumor Photothermal Therapy. *Advanced Functional Materials* **2020,** *30* (50), 2001566.

(8) Zhou, J.; Creyer, M. N.; Chen, A.; Yim, W.; Lafleur, R. P. M.; He, T.; Lin, Z.; Xu, M.; Abbasi, P.; Wu, J.; Pascal, T. A.; Caruso, F.; Jokerst, J. V., Stereoselective Growth of Small Molecule Patches on Nanoparticles. *Journal of the American Chemical Society* **2021,** *143* (31), 12138-12144.

(9) Jin, Z.; Mantri, Y.; Retout, M.; Cheng, Y.; Zhou, J.; Jorns, A.; Fajtova, P.; Yim, W.; Moore, C.; Xu, M.; Creyer, M.; Borum, R.; Zhou, J.; Wu, Z.; He, T.; Penny, W.; O'Donoghue, A.; Jokerst, J., A Charge-Switchable Zwitterionic Peptide for Rapid Detection of SARS-CoV-2 Main Protease. *Angewandte Chemie International Edition* **2021,** *e202112995*.

(10) Lee, J. E.; Lee, N.; Kim, T.; Kim, J.; Hyeon, T., Multifunctional Mesoporous Silica Nanocomposite Nanoparticles for Theranostic Applications. *Accounts of Chemical Research* **2011,** *44* (10), 893-902.

(11) Wu, Z.; Zhou, J.; Nkanga, C. I.; Jin, Z.; He, T.; Borum, R. M.; Yim, W.; Zhou, J.; Cheng, Y.; Xu, M.; Steinmetz, N. F.; Jokerst, J. V., One-Step Supramolecular Multifunctional Coating on Plant Virus Nanoparticles for Bioimaging and Therapeutic Applications. *ACS Appl Mater Interfaces* **2022,** *14* (11), 13692-13702.

(12) Du, L.; Nosratabad, N. A.; Jin, Z.; Zhang, C.; Wang, S.; Chen, B.; Mattoussi, H., Luminescent Quantum Dots Stabilized by N-Heterocyclic Carbene Polymer Ligands. *Journal of the American Chemical Society* **2021,** *143* (4), 1873-1884.

(13) Wang, S.; Du, L.; Jin, Z.; Xin, Y.; Mattoussi, H., Enhanced Stabilization and Easy Phase Transfer of $CsPbBr_3$ Perovskite Quantum Dots Promoted by High-Affinity Polyzwitterionic Ligands. *Journal of the American Chemical Society* **2020,** *142* (29), 12669-12680.

(14) Zhan, N.; Palui, G.; Merkl, J.-P.; Mattoussi, H., Bio-orthogonal Coupling as a Means of Quantifying the Ligand Density on Hydrophilic Quantum Dots. *Journal of the American Chemical Society* **2016,** *138* (9), 3190-3201.

(15) Ding, Z.; Sun, H.; Ge, S.; Cai, Y.; Yuan, Y.; Hai, Z.; Tao, T.; Hu, J.; Hu, B.; Wang, J.; Liang, G., Furin-Controlled Fe_3O_4 Nanoparticle Aggregation and 19F Signal "Turn-On" for Precise MR Imaging of Tumors. *Advanced Functional Materials* **2019,** *29* (43), 1903860.

(16) Wang, Y.; Li, X.; Chen, P.; Dong, Y.; Liang, G.; Yu, Y., Enzyme-instructed self-aggregation of Fe_3O_4 nanoparticles for enhanced MRI T_2 imaging and photothermal therapy of tumors. *Nanoscale* **2020,** *12* (3), 1886-1893.

(17) Jokerst, J. V.; Khademi, C.; Gambhir, S. S., Intracellular Aggregation of Multimodal Silica Nanoparticles for Ultrasound-Guided Stem Cell Implantation. *Science Translational Medicine* **2013,** *5* (177), 177ra35-177ra35.

(18) Cheng, P.; Pu, K., Molecular imaging and disease theranostics with renal-clearable optical agents. *Nature Reviews Materials* **2021,** *6* (12), 1095-1113.

(19) Park, J. H.; Gu, L.; von Maltzahn, G.; Ruoslahti, E.; Bhatia, S. N.; Sailor, M. J., Biodegradable luminescent porous silicon nanoparticles for in vivo applications. *Nat Mater* **2009,** *8* (4), 331-6.

(20) Liew, S. S.; Zeng, Z.; Cheng, P.; He, S.; Zhang, C.; Pu, K., Renal-Clearable Molecular Probe for Near-Infrared Fluorescence Imaging and Urinalysis of SARS-CoV-2. *Journal of the American Chemical Society* **2021,** *143* (45), 18827-18831.

(21) Huang, J.; Jiang, Y.; Li, J.; He, S.; Huang, J.; Pu, K., A Renal-Clearable Macromolecular Reporter for Near-Infrared Fluorescence Imaging of Bladder Cancer. *Angewandte Chemie International Edition* **2020,** *59* (11), 4415-4420.

(22) Nafiujjaman, M.; Chung, S.-J.; Kalashnikova, I.; Hill, M. L.; Homa, S.; George, J.; Contag, C. H.; Kim, T., Biodegradable Hollow Manganese Silicate Nanocomposites to Alleviate Tumor Hypoxia toward Enhanced Photodynamic Therapy. *ACS Applied Bio Materials* **2020,** *3* (11), 7989-7999.

(23) Lyu, Y.; Zeng, J.; Jiang, Y.; Zhen, X.; Wang, T.; Qiu, S.; Lou, X.; Gao, M.; Pu, K., Enhancing Both Biodegradability and Efficacy of Semiconducting Polymer Nanoparticles for Photoacoustic Imaging and Photothermal Therapy. *ACS Nano* **2018,** *12* (2), 1801-1810.

(24) Liang, Y.; Sun, H.; Cao, W.; Thompson, M. P.; Gianneschi, N. C., Degradable Polyphosphoramidate via Ring-Opening Metathesis Polymerization. *ACS Macro Letters* **2020,** *9* (10), 1417-1422.

(25) Lovell, J. F.; Jin, C. S.; Huynh, E.; MacDonald, T. D.; Cao, W.; Zheng, G., Enzymatic Regioselection for the Synthesis and Biodegradation of Porphysome Nanovesicles. *Angewandte Chemie International Edition* **2012,** *51* (10), 2429-2433.

(26) Sun, H.; Liang, Y.; Thompson, M. P.; Gianneschi, N. C., Degradable polymers via olefin metathesis polymerization. *Progress in Polymer Science* **2021,** *120*, 101427.

(27) Sun, H.; Yan, L.; Carter, K. A.; Zhang, J.; Caserto, J. S.; Lovell, J. F.; Wu, Y.; Cheng, C., Zwitterionic Cross-Linked Biodegradable Nanocapsules for Cancer Imaging. *Langmuir* **2019,** *35* (5), 1440-1449.

(28) Sun, H.; Yan, L.; Chang, M. Y. Z.; Carter, K. A.; Zhang, R.; Slyker, L.; Lovell, J. F.; Wu, Y.; Cheng, C., A multifunctional biodegradable brush polymer-drug conjugate for paclitaxel/gemcitabine co-delivery and tumor imaging. *Nanoscale Advances* **2019,** *1* (7), 2761-2771.

(29) Altınogˇlu, E. I.; Russin, T. J.; Kaiser, J. M.; Barth, B. M.; Eklund, P. C.; Kester, M.; Adair, J. H., Near-infrared emitting fluorophore-doped calcium phosphate nanoparticles for in vivo imaging of human breast cancer. *ACS Nano* **2008,** *2* (10), 2075-2084.

(30) Tang, J.; Li, L.; Howard, C. B.; Mahler, S. M.; Huang, L.; Xu, Z. P., Preparation of optimized lipid-coated calcium phosphate nanoparticles for enhanced in vitro gene delivery to breast cancer cells. *Journal of Materials Chemistry B* **2015,** *3* (33), 6805-6812.

(31) Liu, Z.; Xiao, Y.; Chen, W.; Wang, Y.; Wang, B.; Wang, G.; Xu, X.; Tang, R., Calcium phosphate nanoparticles primarily induce cell necrosis through lysosomal rupture: the origination of material cytotoxicity. *Journal of Materials Chemistry B* **2014,** *2* (22), 3480-3489.

(32) Abou Neel, E. A.; Pickup, D. M.; Valappil, S. P.; Newport, R. J.; Knowles, J. C., Bioactive functional materials: a perspective on phosphate-based glasses. *Journal of Materials Chemistry* **2009,** *19* (6), 690-701.

(33) Knowles, J. C., Phosphate based glasses for biomedical applications. *Journal of Materials Chemistry* **2003,** *13* (10), 2395.

(34) Foroutan, F.; Jokerst, J. V.; Gambhir, S. S.; Vermesh, O.; Kim, H.-W.; Knowles, J. C., Sol–Gel Synthesis and Electrospraying of Biodegradable $(P_2O_5)_{55}$–$(CaO)_{30}$–$(Na_2O)_{15}$ Glass Nanospheres as a Transient Contrast Agent for Ultrasound Stem Cell Imaging. *ACS Nano* **2015,** *9* (2), 1868-1877.

(35) Santos, E. M.; Radin, S.; Ducheyne, P., Sol-gel derived carrier for the controlled release of proteins. *Biomaterials* **1999,** *20* (18), 1695-700.

(36) Govindan, R.; Girija, E. K., Drug loaded phosphate glass/hydroxyapatite nanocomposite for orthopedic applications. *J Mater Chem B* **2014,** *2* (33), 5468-5477.

(37) Casciaro, S.; Conversano, F.; Ragusa, A.; Ada Malvindi, M.; Franchini, R.; Greco, A.; Pellegrino, T.; Gigli, G., Optimal Enhancement Configuration of Silica Nanoparticles for Ultrasound Imaging and Automatic Detection at Conventional Diagnostic Frequencies. *Investigative Radiology* **2010,** *45* (11).

(38) Errico, C.; Pierre, J.; Pezet, S.; Desailly, Y.; Lenkei, Z.; Couture, O.; Tanter, M., Ultrafast ultrasound localization microscopy for deep super-resolution vascular imaging. *Nature* **2015,** *527* (7579), 499-502.

(39) Demené, C.; Robin, J.; Dizeux, A.; Heiles, B.; Pernot, M.; Tanter, M.; Perren, F., Transcranial ultrafast ultrasound localization microscopy of brain vasculature in patients. *Nature Biomedical Engineering* **2021,** *5* (3), 219-228.

(40) He, T.; Bradley, D. G.; Zhou, J.; Jorns, A.; Mantri, Y.; Hanna, J. V.; Jokerst, J. V., Hydro-Expandable Calcium Phosphate Micro/Nano-Particles with Controllable Size and Morphology for Mechanical Ablation. *ACS Applied Nano Materials* **2021,** *4* (4), 3877-3886.

(41) He, T.; Jokerst, J. V., Structured micro/nano materials synthesized via electrospray: a review. *Biomaterials Science* **2020,** *8* (20), 5555-5573.

(42) Sumper, M.; Brunner, E., Learning from Diatoms: Nature's Tools for the Production of Nanostructured Silica. *Advanced Functional Materials* **2006,** *16* (1), 17-26.

(43) Sumper, M.; Kröger, N., Silica formation in diatoms: the function of long-chain polyamines and silaffins. *Journal of Materials Chemistry* **2004,** *14* (14), 2059-2065.

(44) Antonietti, L.; Aymonier, C.; Schlotterbeck, U.; Garamus, V. M.; Maksimova, T.; Richtering, W.; Mecking, S., Core−Shell-Structured Highly Branched Poly(ethylenimine amide)s: Synthesis and Structure. *Macromolecules* **2005,** *38* (14), 5914-5920.

(45) Lei, Q.; Guo, J.; Kong, F.; Cao, J.; Wang, L.; Zhu, W.; Brinker, C. J., Bioinspired Cell Silicification: From Extracellular to Intracellular. *Journal of the American Chemical Society* **2021,** *143* (17), 6305-6322.

(46) Pickup, D. M.; Guerry, P.; Moss, R. M.; Knowles, J. C.; Smith, M. E.; Newport, R. J., New sol–gel synthesis of a $(CaO)_{0.3}(Na_2O)_{0.2}(P_2O_5)_{0.5}$ bioresorbable glass and its structural characterisation. *Journal of Materials Chemistry* **2007,** *17* (45), 4777.

(47) Benjaminsen, R. V.; Mattebjerg, M. A.; Henriksen, J. R.; Moghimi, S. M.; Andresen, T. L., The Possible "Proton Sponge" Effect of Polyethylenimine (PEI) Does Not Include Change in Lysosomal pH. *Molecular Therapy* **2013,** *21* (1), 149-157.

(48) Yeh, P.-H.; Sun, J.-S.; Wu, H.-C.; Hwang, L.-H.; Wang, T.-W., Stimuli-responsive HA-PEI nanoparticles encapsulating endostatin plasmid for stem cell gene therapy. *RSC advances* **2013,** *3* (31), 12922-12932.

(49) Jin, Z.; Du, L.; Zhang, C.; Sugiyama, Y.; Wang, W.; Palui, G.; Wang, S.; Mattoussi, H., Modification of poly (maleic anhydride)-based polymers with H_2N–R nucleophiles: Addition or substitution reaction? *Bioconjugate chemistry* **2019,** *30* (3), 871-880.

(50) Catti, M.; Ferraris, G.; Filhol, A., Hydrogen bonding in the crystalline state. $CaHPO_4$ (monetite), P1 or P1? A novel neutron diffraction study. *Acta Crystallographica Section B Structural Crystallography and Crystal Chemistry* **1977,** *33* (4), 1223--1229.

(51) Curry, N. A.; Jones, D. W., Crystal structure of brushite, calcium hydrogen orthophosphate dihydrate: a neutron-diffraction investigation. *Journal of the Chemical Society A: Inorganic, Physical, Theoretical* **1971**, 10.1039/J19710003725 (0), 3725--3729.

(52) Dickens, B.; Prince, E.; Schroeder, L. W.; Brown, W. E., $Ca(H_2PO_4)_2$, a crystal structure containing unusual hydrogen bonding. *Acta Crystallographica Section B Structural Crystallography and Crystal Chemistry* **1973,** *29* (10), 2057--2070.

(53) Liu, S.; Liang, Y.; Ma, X.; Li, H.; Zhang, W.; Tu, D.; Chen, Y., Tunable Photoluminescence and Energy Transfer Efficiency in β-$Ca_3(PO_4)_2$-$Ca_9La(PO_4)_7$:Eu^{2+}, Mn^{2+} Solid Solution Phosphors Introduced by Emptying Site and Structural Confinement Effect for Solid-State Lighting Application. *Inorganic Chemistry* **2020,** *59* (6), 3596--3605.

(54) Mathew, M.; Brown, W. E.; Schroeder, L. W.; Dickens, B., Crystal structure of octacalcium bis(hydrogenphosphate) tetrakis(phosphate)pentahydrate, $Ca_8(HPO_4)_2(PO_4)_4 \cdot 5H_2O$. *Journal of Crystallographic and Spectroscopic Research 1988 18:3* **1988,** *18* (3), 235--250.

(55) Mathew, M.; Schroeder, L. W.; Dickens, B.; Brown, W. E., The crystal structure of α-$Ca_3(PO_4)_2$. *Acta Crystallographica Section B* **1977,** *33* (5), 1325--1333.

(56) Schroeder, L. W.; Prince, E.; Dickens, B.; Iucr, Hydrogen bonding in $Ca(H_2PO_4)_2.H_2O$ as determined by neutron diffraction. *Acta Crystallographica Section B* **1975,** *31* (1), 9--12.

(57) Tanaka, Y.; Iwasaki, T.; Katayama, K.; Hojo, J.; Yamashita, K., Effect of Ionic Polarization on Crystal Structure of Hydroxyapatite Ceramic with Hydroxide Nonstoichiometry. *Journal of the Japan Society of Powder and Powder Metallurgy* **2010,** *57* (7), 520--528.

(58) Brow, R. K., Review: the structure of simple phosphate glasses. *Journal of Non-Crystalline Solids* **2000,** *263-264*, 1-28.

(59) Sirsi, S.; Feshitan, J.; Kwan, J.; Homma, S.; Borden, M., Effect of microbubble size on fundamental mode high frequency ultrasound imaging in mice. *Ultrasound in medicine & biology* **2010,** *36* (6), 935-948.

(60) Casciaro, S.; Conversano, F.; Ragusa, A.; Ada Malvindi, M.; Franchini, R.; Greco, A.; Pellegrino, T.; Gigli, G., Optimal Enhancement Configuration of Silica Nanoparticles for Ultrasound Imaging and Automatic Detection at Conventional Diagnostic Frequencies. *Investigative Radiology* **2010,** *45* (11), 715-724.

(61) Pastor‐Pérez, L.; Chen, Y.; Shen, Z.; Lahoz, A.; Stiriba, S. E., Unprecedented Blue Intrinsic Photoluminescence from Hyperbranched and Linear Polyethylenimines: Polymer Architectures and pH‐Effects. *Macromolecular rapid communications* **2007,** *28* (13), 1404-1409.

(62) Kempen, P. J.; Greasley, S.; Parker, K. A.; Campbell, J. L.; Chang, H. Y.; Jones, J. R.; Sinclair, R.; Gambhir, S. S.; Jokerst, J. V., Theranostic mesoporous silica nanoparticles biodegrade after pro-survival drug delivery and ultrasound/magnetic resonance imaging of stem cells. *Theranostics* **2015,** *5* (6), 631-42.

(63) Hunter, A. C., Molecular hurdles in polyfectin design and mechanistic background to polycation induced cytotoxicity. *Advanced drug delivery reviews* **2006,** *58* (14), 1523-31.

(64) Gottlieb, H. E.; Kotlyar, V.; Nudelman, A., NMR chemical shifts of common laboratory solvents as trace impurities. *Journal of Organic Chemistry* **1997,** *62* (21), 7512-7515.

(65) Huang, X.; Zhu, Y.; Zhang, X.; Bao, Z.; Lei, D. Y.; Yu, W.; Dai, J.; Wang, Y., Clam-inspired nanoparticle immobilization method using adhesive tape as microchip substrate. *Sensors and Actuators B: Chemical* **2016,** *222*, 106-111.

TABLE OF CONTENTS

Mimicking the bio-silicification process found in diatoms, we demonstrated the sol-gel reaction using polyethylenimine (PEI) to template phosphate esters and producing PEI/calcium phosphate (CP) with versatile sizes (396±128 nm to 63±8 μm) and morphologies (hexagonal micro-disc, micro-flower, micro-leaf, nano-butterfly, and nano-ribbon). PEI/CPs have intrinsic photoluminescence, strong echogenicity, and excellent biodegradability and may be used for transient ultrasound imaging.